

# Binary interaction dominates mass ejection in classical novae

KEN J. SHEN<sup>1</sup> AND ELIOT QUATAERT<sup>2</sup>

<sup>1</sup>*Department of Astronomy and Theoretical Astrophysics Center, University of California, Berkeley, CA 94720, USA*  
<sup>2</sup>*Department of Astrophysical Sciences, Princeton University, Princeton, NJ 08544, USA*

## ABSTRACT

Recent observations suggest our understanding of mass loss in classical novae is incomplete, motivating a new theoretical examination of the physical processes responsible for nova mass ejection. In this paper, we perform hydrodynamical simulations of classical nova outflows using the stellar evolution code MESA. We find that, when the binary companion is neglected, white dwarfs with masses  $\gtrsim 0.8 M_{\odot}$  successfully launch radiation-pressure-driven optically thick winds that carry away most of the envelope. However, for most of the mass loss phase, these winds are accelerated at radii beyond the white dwarf’s Roche radius assuming a typical cataclysmic variable donor. This means that, before a standard optically thick wind can be formed, mass loss will instead be initiated and shaped by the binary interaction. An isotropic optically thick wind is only successfully launched when the acceleration region recedes within the white dwarf’s Roche radius, which occurs after most of the envelope has already been ejected. The interaction between these two modes of outflow – a first phase of slow, binary-driven, equatorially focused mass loss encompassing most of the mass ejection and a second phase consisting of a fast, isotropic, optically thick wind – is consistent with observations of aspherical ejecta and signatures of multiple outflow components. We also find that isolated lower-mass white dwarfs  $\lesssim 0.8 M_{\odot}$  do not develop unbound optically thick winds at any stage, making it even more crucial to consider the effects of the binary companion on the resulting outburst.

*Keywords:* binaries: close— nuclear reactions, nucleosynthesis, abundances— novae, cataclysmic variables— white dwarfs

## 1. INTRODUCTION AND THE PHYSICS OF CLASSICAL NOVA OUTBURSTS

A classical nova outburst results from the ignition of a hydrogen-rich envelope on a white dwarf (WD) accreted from a binary companion in a cataclysmic variable (CV) system (see Bode & Evans 2008 and Chomiuk et al. 2021 for reviews).<sup>1</sup> Once a sufficient envelope mass has been accumulated ( $\sim 10^{-4} - 10^{-6} M_{\odot}$ , depending on properties such as the accretion rate and the WD mass and temperature; Prialnik & Kovetz 1995; Townsley & Bildsten 2004; Yaron et al. 2005), thermonuclear fusion of the hydrogen-rich fuel generates energy faster than it can diffuse away, and a convective burning shell is born.

This convective zone heats on a timescale given by the ratio of the envelope’s internal energy to its nuclear

luminosity:

$$\begin{aligned}
t_{\text{heat}} &= \frac{\int_{M_{\text{core}}}^{M_{\text{total}}} c_P T dm}{\int_{M_{\text{core}}}^{M_{\text{total}}} \epsilon dm} \sim f \frac{c_{P,\text{base}} T_{\text{base}}}{\epsilon_{\text{base}}} \\
&\sim 10 \text{ yr} \left( \frac{f}{4} \right) \left( \frac{0.6}{X} \right) \left( \frac{0.2}{Z_{\text{CNO}}} \right) \\
&\quad \times \left( \frac{3 \times 10^3 \text{ g cm}^{-3}}{\rho_{\text{base}}} \right) \left( \frac{T_{\text{base}}}{3 \times 10^7 \text{ K}} \right)^{5/3} \\
&\quad \times \exp \left[ \frac{49.008}{(T_{\text{base}}/3 \times 10^7 \text{ K})^{1/3}} - 49.008 \right], \quad (1)
\end{aligned}$$

where the total mass,  $M_{\text{total}}$ , is the sum of the underlying core mass,  $M_{\text{core}}$ , and the outbursting envelope mass,  $M_{\text{env}}$ . The factor of  $f \sim 4$  is estimated from simulations described later in this paper and approximately accounts for the extent of the burning region being smaller than the region encompassing the bulk of the internal energy in the convective zone. The subscript “base” refers to quantities evaluated at the base of the envelope, the specific heat at constant pressure,  $c_P$ , is assumed to be the ideal gas value,  $5k/2\mu m_p$  (as

<sup>1</sup> Recurrent novae are novae with short enough recurrence times that multiple outbursts have been observed in human history. Novae in symbiotic systems arise from the same basic physics, but they occur in much more widely separated binaries with giant donors.

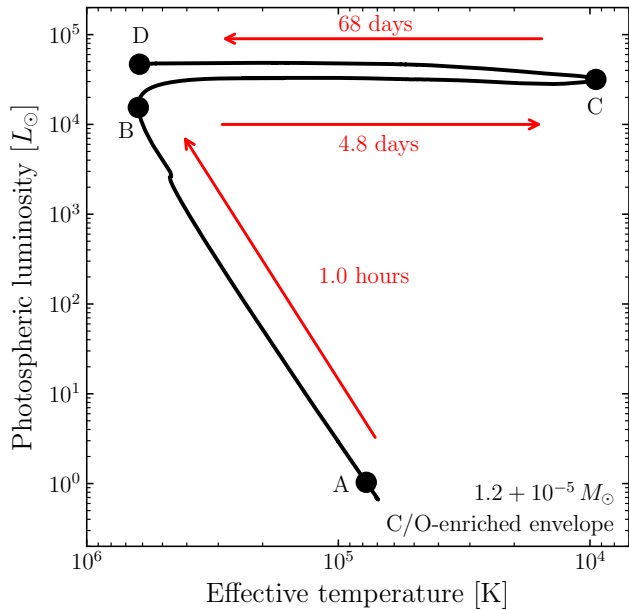


**Figure 1.** Photospheric luminosity vs. effective temperature for a simulation of a  $1.2 M_{\odot}$  WD with a  $10^{-5} M_{\odot}$  C/O-enriched outbursting nova envelope. The model is evolved with MESA and does not include any effects of a companion star. See Sections 2 and 3 for more details.

roughly appropriate at the onset of convection), and the energy generation rate,  $\epsilon$ , is evaluated in the cold CNO limit, where the  $^{14}\text{N}+p$  reaction is the rate-limiting step (Lemut et al. 2006). The fiducial values of the hydrogen mass fraction,  $X$ , and the CNO mass fraction,  $Z_{\text{CNO}}$ , are representative of a C/O-enriched envelope, as commonly observed in nova ejecta (Gehrz et al. 1998).

The heating convective zone grows outwards in mass (and perhaps inwards as well if convective dredge-up and overshooting are efficient). As the outer edge of the convective zone nears the photosphere, radiation is able to diffuse out of the star, the photospheric luminosity increases dramatically, and the WD climbs back up the WD cooling sequence with a roughly constant radius. Figure 1 shows the evolution in the Hertzsprung-Russell diagram of a model of a  $1.2 M_{\odot}$  WD with a  $10^{-5} M_{\odot}$  outbursting envelope that is enriched with 10%  $^{12}\text{C}$  and 10%  $^{16}\text{O}$  by mass (see Sections 2 and 3 for simulation details). This initial phase of rising luminosity between point A, where the photospheric luminosity is  $1 L_{\odot}$ , and point B, the time of maximum effective temperature,  $T_{\text{eff}}$ , happens very rapidly for this case, with the luminosity increasing by four orders of magnitude in just one hour.

This brightening continues until the radiative luminosity nears the Eddington limit,

$$L_{\text{Edd}} = \frac{4\pi GM_{\text{core}}c}{\kappa} = 1.7 \times 10^{38} \text{ erg s}^{-1} \left( \frac{M_{\text{core}}}{M_{\odot}} \right) \left( \frac{0.3 \text{ cm}^2 \text{ g}^{-1}}{\kappa} \right), \quad (2)$$

where the mass of the WD core dominates the total mass of the star, and  $\kappa$  is the opacity. After this point, the envelope expands at a roughly constant luminosity, causing the effective temperature to decrease from its maximum value. The brief time spent near the maximum effective temperature leads to a short-lived ultraviolet or X-ray nova precursor, depending on the WD mass, as calculated by Hillman et al. (2014) and observed in the ultraviolet by Cao et al. (2012) and in the X-rays by König et al. (2022). It is important to note that initially, this phase of expansion is relatively gentle and essentially hydrostatic for most of the envelope’s mass, with expansion velocities that are slower than the local speed of sound.

For cases where the convective turnover timescale is short enough, convection will transport  $\beta$ -unstable nuclei ( $^{13}\text{N}$ ,  $^{14}\text{O}$ ,  $^{15}\text{O}$ , and  $^{17}\text{F}$ ) from CNO-burning at the base of the envelope up to the outer layers before they have had a chance to decay. If there is significant pollution of the envelope by core material rich in carbon and oxygen, the energy generation rate from these decays will be sufficient to directly eject material from the outer layers at high velocities  $> 1000 \text{ km s}^{-1}$  (Starrfield et al. 2016 and references therein); for the model shown in Figure 1, no material is lost in this way. We discuss this ejection mechanism further in Section 3, but we note here that when it does occur, it only unbinds a small amount of material. The vast majority of the envelope mass during this stage expands slowly and remains bound to the WD.

The rest of the nova envelope, minus any small mass unbound by the surface  $\beta$ -decays, continues to expand until one of two things happens: either the envelope overflows the WD’s Roche lobe and encounters the companion’s gravitational potential, or an optically thick wind is launched. Most previous theoretical studies of classical nova outbursts have chosen to neglect the binary companion and have focused on the second outcome. We now briefly review the sequence of events that arises if the companion is neglected before highlighting observational challenges to this picture.

Once the envelope has expanded sufficiently, part of it will traverse a peak in the opacity at a temperature of  $\sim 1.5 \times 10^5 \text{ K}$  due to bound-bound transitions of

iron-group elements (Iglesias et al. 1990). This “iron opacity bump” results in a localized trough in the Eddington luminosity, causing the luminosity to become super-Eddington even though its absolute value stays constant. Radiative diffusion is no longer sufficient to carry the luminosity, so convection sets in. However, the inferred convective velocity from mixing-length theory required to carry this high flux is supersonic, and thus convection is insufficient to transport the luminosity. Instead, an optically thick wind is formed, which drives a sustained outflow that ejects most of the nova envelope.

During this phase, the photospheric radius first increases until a minimum effective temperature is reached (corresponding to the 5-day evolution between points B and C for the model shown in Fig. 1), and then, as envelope mass is lost, the photosphere recedes. This phase is the longest of the outburst, taking 68 d for the model in Figure 1 to evolve between points C and D.

Once the envelope mass has decreased to the maximal envelope mass that can support a thin, steadily burning, thermally stable hydrostatic solution (Fujimoto 1982; Nomoto et al. 2007; Shen & Bildsten 2007; Wolf et al. 2013), mass loss ends. The remaining bound envelope continues to fuse hydrogen at its base, emitting as a supersoft X-ray source due to the contraction of the photosphere. However, the actual appearance of the nova system may not match the WD’s emission due to obscuration by the previous phase of mass ejection. Eventually, the consumption of fuel reduces the envelope mass below the minimum stable solution, burning ceases, and the WD evolves back down the cooling sequence. Continued accretion provides a fresh source of hydrogen-rich fuel until enough has accumulated to trigger the next nova outburst, and the cycle begins again.

Having reviewed the standard picture of mass loss due to near-Eddington winds, we now summarize observational evidence that has mounted against the main assumption of a spherically symmetric, optically thick wind being the main driver of nova mass loss (Chomiuk et al. 2021). Resolved imaging of novae during eruption (Chomiuk et al. 2014) and years and decades afterwards (e.g., Slavin et al. 1995; Sokolowski et al. 2017) shows clear evidence for aspherical ejecta and multiple modes of mass ejection. This is also seen in spectral indicators (e.g., Aydi et al. 2020a) and the detection of shock interaction in many nearby classical novae (Ackermann et al. 2014; Weston et al. 2016; Finzell et al. 2018; Nelson et al. 2019; Aydi et al. 2020b; Sokolovsky et al. 2020). Optically thick winds also fail to explain the super-Eddington luminosities (e.g., Schwarz et al. 2001; Aydi et al. 2018)

and the wide variety of behaviors (Strope et al. 2010) demonstrated by some nova light curves.

In this study, we perform hydrodynamical simulations of classical nova outbursts on isolated WDs using the stellar evolution code MESA (Paxton et al. 2011, 2013, 2015, 2018). Our results confirm the previously described sequence of events for the launching of optically thick winds for WD masses  $\gtrsim 0.8 M_{\odot}$ . However, for lower-mass WDs, none of the models we run achieves a successful wind solution; instead, the envelope remains bound for its entire evolution as the wind is either choked or is never launched at all.

Crucially, we find that, even for successful winds, the velocity at the location of the WD’s Roche radius is slower than the typical orbital velocities of WDs in CVs for most of the mass loss phase, because the acceleration region is outside of the WD’s Roche lobe. As a result, standard optically thick winds cannot form, and binary interaction will instead initiate the majority of mass loss, focusing it towards the equatorial plane. It is only during the final stages of the nova outburst, when the acceleration region recedes within the WD’s Roche lobe, that a spherical optically thick wind can form. The interaction of this fast, isotropic wind with the prior phase of slow, equatorial outflow is likely responsible for the previously outlined observations of aspherical, self-interacting ejecta.

There have been numerous MESA studies of various properties of classical nova systems (e.g., Denissenkov et al. 2013, 2014; Wolf et al. 2013, 2018; Chen et al. 2019; Ginzburg & Quataert 2021; Leung & Siegert 2021; Guo et al. 2022), but the present work is the first to use it to study hydrodynamical nova outflows. We outline our simulations in Section 2 and describe our results in Section 3. We compare to previous studies of nova outbursts in Section 4. We summarize our findings and discuss their broader implications in Section 5.

## 2. DESCRIPTION OF SIMULATIONS

We use MESA<sup>2</sup> to evolve nova outbursts, assuming no interaction with a companion star, for a range of WD core masses (0.6, 0.8, 1.0, and 1.2  $M_{\odot}$ ) and envelope masses that bracket the expected ignition masses found by evolutionary calculations (Priyalnik & Kovetz 1995; Townsley & Bildsten 2004; Yaron et al. 2005; Denissenkov et al. 2013). We ignore the pre-outburst accretion history and instead take the mass coordinate of the base of the convective zone during the outburst as a given. We thus avoid the difficulty of setting up the cor-

<sup>2</sup> <http://mesa.sourceforge.net>, version 10398; default options used unless otherwise noted.

rect equilibrium conditions of the underlying core, which depend on many factors including the ages of the WD and CV, and which otherwise play an important role in determining the ignition mass of the outbursting envelope (Townsend & Bildsten 2004; Epelstein et al. 2007).

We are also agnostic to the details of the envelope’s enrichment with core material, which is frequently observed in nova ejecta (Gehrz et al. 1998) and may occur a variety of ways, including chemical diffusion (Prialnik & Kovetz 1984, 1995; Kovetz & Prialnik 1985; Yaron et al. 2005), rotationally induced shear mixing (Kippenhahn & Thomas 1978; Livio & Truran 1987; Kutter & Sparks 1989; Alexakis et al. 2004), and convectively induced shear mixing and overshooting (Woosley 1986; Glasner & Livne 1995; Glasner et al. 1997, 2012; Rosner et al. 2001; Casanova et al. 2010, 2011a,b, 2016, 2018). As with the envelope mass, we take the envelope composition as a given because of uncertainties in the strengths of the various enrichment mechanisms and explore two compositions: solar composition (Asplund et al. 2009), which is equivalent to the assumption that no mixing occurs with the underlying C/O core, and an enhanced C/O composition, with 80% solar composition by mass plus an additional 10% by mass of  $^{12}\text{C}$  and  $^{16}\text{O}$  each. The composition of the accreted material may not be solar, which can induce changes to the ignition mass (Piersanti et al. 2000; Starrfield et al. 2000; José & Hernanz 2007; Shen & Bildsten 2009; Chen et al. 2019; Kemp et al. 2022; Hillman & Gerbi 2022), but since we parametrize the convective envelope masses by hand in this study, we bypass this complication.

We construct our WD models by first creating pure C/O objects with specified masses between  $0.6$  and  $1.2 M_{\odot}$  with nuclear burning disabled. To prevent spurious numerical mixing between the envelope and the core during the outburst, which would further enrich the envelope with C/O, we accrete a  $10^{-4} M_{\odot}$  pure  $^4\text{He}$  buffer before adding the envelope with the desired composition and mass. We specify the mass fractions of  $^1\text{H}$ ,  $^4\text{He}$ ,  $^{12}\text{C}$ ,  $^{14}\text{N}$ , and  $^{16}\text{O}$  in the envelope material. The entire star is then allowed to cool until the center reaches  $2 \times 10^7$  K, and nuclear burning is turned back on. We use the `cno_extras` burning network, which includes  $^1\text{H}$ ,  $^3\text{--}^4\text{He}$ ,  $^{12\text{--}13}\text{C}$ ,  $^{13\text{--}15}\text{N}$ ,  $^{14\text{--}18}\text{O}$ ,  $^{17\text{--}19}\text{F}$ ,  $^{18\text{--}20}\text{Ne}$ , and  $^{22,24}\text{Mg}$ , and the reactions linking them with rates from the JINA Reaclib database (Cyburt et al. 2010).

Due to the low temperatures resulting from cooling the entire star, most models do not experience a convective thermonuclear runaway when nuclear burning is turned on. We thus input extra heating at the base of the envelope until the convective burning is self-sustained, at which point the extra heating is turned off.

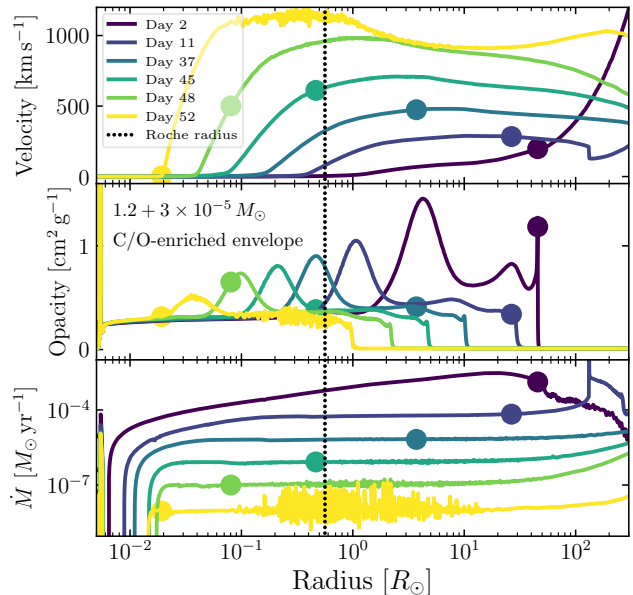


**Figure 2.** Velocity (top panel), opacity (middle panel), and mass flux (bottom panel) profiles for the  $1.2 + 3 \times 10^{-5} M_{\odot}$  C/O-enriched envelope calculation. The location of the  $\tau = 2/3$  photosphere is shown as a circle for each profile, and the location of the Roche radius assuming a  $0.3 M_{\odot}$ ,  $0.3 R_{\odot}$  Roche-lobe-filling donor is shown as a dotted line. Times are given with respect to the time of maximum effective temperature.

Once convective burning begins, we enable a variety of flags in MESA to follow the hydrodynamic evolution of the outburst. Further details regarding this implementation and the inlists used for the calculations are located in the Appendix.

Simulations that result in successful optically thick winds are evolved until the mass outflow begins to cease, at which point numerical issues lead to small timesteps and the simulations are ended. Models that do not launch winds enter a long-lived steady state and are halted after several weeks of computational time.

### 3. SIMULATION RESULTS

#### 3.1. Models with successful winds

In Figures 2 and 3, we show radial profiles of various quantities of interest for the  $1.2 M_{\odot}$  WD with a C/O-enriched envelope of  $3 \times 10^{-5} M_{\odot}$ . The times of the profiles are given with respect to the time of maximum effective temperature. The profile at day 2 shows evidence of high velocity ejection in the outer layers, with velocities surpassing  $10^3 \text{ km s}^{-1}$ . This is due to the convective mixing of  $\beta$ -unstable nuclei (primarily  $^{13}\text{N}$  and  $^{15}\text{O}$ ) into the surface layers of the star at a time when the surface has expanded enough for the decay energy to be sufficient to unbind material (see Starrfield



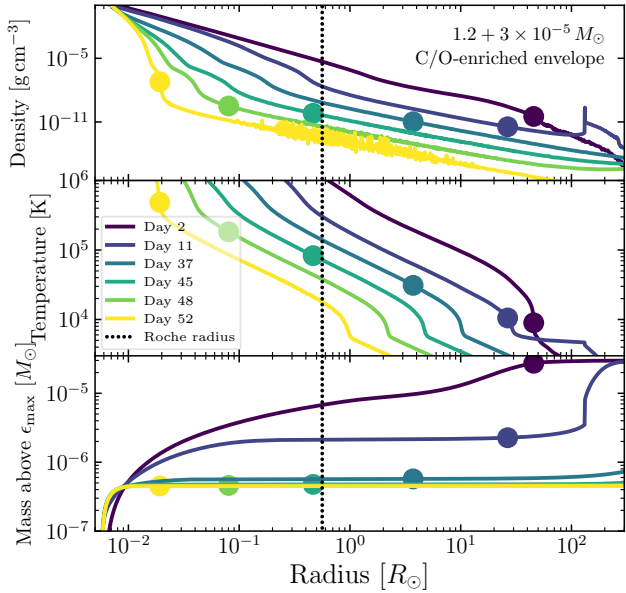


**Figure 3.** Same as Fig. 2, but showing radial profiles of the density (top panel), temperature (middle panel), and mass above the location of maximum energy generation (bottom panel). Comparison of Figs. 2 and 3 shows that most of the envelope is lost between days 2 – 11 when the outflow velocities at the Roche radius are low. In reality, binary interactions thus dominate the properties of the ejected mass.

et al. 2016 and references therein). However, such a phase only lasts a short duration before convection recedes from the surface layers. As a result, only a very small amount of mass ( $< 10^{-7} M_{\odot}$ ) reaches velocities  $> 1000 \text{ km s}^{-1}$  at the beginning of this simulation. Furthermore, C/O enrichment is necessary to yield enough  $\beta$ -unstable nuclei and subsequent sufficient specific energy release to power this initial outflow; the  $1.2 M_{\odot}$  WD with a solar composition  $3 \times 10^{-5} M_{\odot}$  envelope does not exhibit this outer layer of fast-moving material. The only other simulations that result in an initial phase of rapidly moving surface layers are the most massive C/O-enriched envelopes for each WD mass, but, as for the  $1.2 + 3 \times 10^{-5} M_{\odot}$  model, in each case,  $< 10^{-7} M_{\odot}$  reaches velocities of  $1000 \text{ km s}^{-1}$ . This initial phase of rapid mass ejection is thus more important for larger envelope masses and higher C/O enrichment. Future work will examine these effects, but it appears to make a very small contribution to the total mass lost during typical novae.

By day 11, a steady-state optically thick wind has been established, with a mass flux that is constant through most of the envelope. The acceleration region coincides with the iron opacity bump. While most of the envelope has adjusted itself to be somewhat sub-Eddington with respect to electron-scattering opacity,

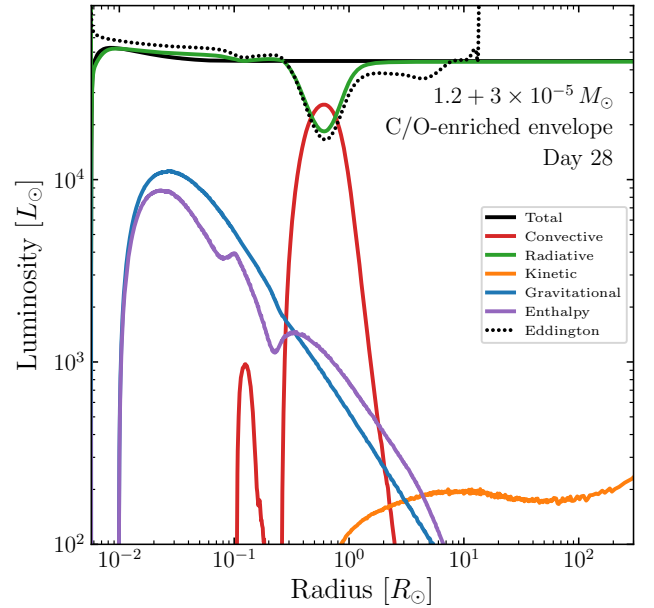


**Figure 4.** Radial profiles of various luminosities, as labeled, for the  $1.2 + 3 \times 10^{-5} M_{\odot}$  C/O-enriched envelope model.

the increased opacity at the iron bump leads to a locally super-Eddington luminosity. Convection is active in this region but is inefficient, and as a result, a wind is launched.

Figure 4 shows various luminosities within the  $1.2 + 3 \times 10^{-5} M_{\odot}$ , C/O-enriched envelope model at day 28, during this steady-state, optically thick wind phase. The figure shows the kinetic energy luminosity,  $\dot{M}v^2/2$  (orange), the power required to climb out of the potential well,  $GMM/r$  (blue), the enthalpy luminosity,  $\dot{M}(u + P/\rho)$  (purple), where  $u$  is the mass-specific energy, the radiative luminosity (green), and the convective luminosity (red). The total luminosity,  $\Lambda$  (black), is essentially constant throughout the envelope, as befits this steady-state solution, except for near the envelope base where the nuclear energy generation is located. The iron opacity peak implies a trough in the Eddington luminosity (black dotted line), causing the luminosity to be mildly super-Eddington in that region.

At this time, the asymptotic kinetic power is a small fraction of the total luminosity; most of the nuclear burning luminosity emerges as radiative luminosity during this stage. However, over the lifetime of the nova outburst, the majority of the energy release goes to overcoming the gravitational binding energy prior to and during the establishment of the steady-state wind:  $E_{\text{bind}} \gg E_{\text{lum}}$ , where the energy to unbind most of the

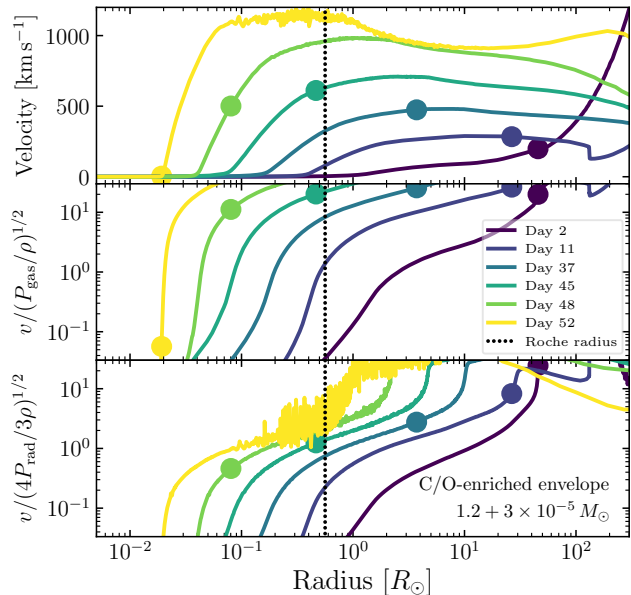


**Figure 5.** Same as Fig. 2, but showing radial profiles of the ratio of the velocity to the isothermal gas sound speed (middle panel) and the ratio of the velocity to the radiation sound speed (bottom panel). The velocity profile is shown again in the top panel for clarity.

nova envelope is

$$\begin{aligned}
 E_{\text{bind}} &\sim \frac{GM_{\text{core}}M_{\text{env}}}{R_0} \\
 &\sim 5.3 \times 10^{46} \text{ erg} \left( \frac{M_{\text{core}}}{M_{\odot}} \right) \left( \frac{M_{\text{env}}}{10^{-4} M_{\odot}} \right) \\
 &\quad \times \left( \frac{5 \times 10^8 \text{ cm}}{R_0} \right), \quad (3)
 \end{aligned}$$

and the total radiated luminosity is

$$\begin{aligned}
 E_{\text{lum}} &\sim L_{\text{Edd}} t_{\text{Edd}} \\
 &\sim 4.3 \times 10^{44} \text{ erg} \left( \frac{M_{\text{core}}}{M_{\odot}} \right) \left( \frac{0.3 \text{ cm}^2 \text{ g}^{-1}}{\kappa} \right) \\
 &\quad \times \left( \frac{t_{\text{nova}}}{1 \text{ month}} \right). \quad (4)
 \end{aligned}$$

The initial WD radius is  $R_0$ , and the time the nova spends near the Eddington luminosity is  $t_{\text{Edd}}$ .

Figure 5 shows the ratio of the velocity to the isothermal gas sound speed (middle panel) and the radiation sound speed (bottom panel) at the same times as in Figures 2 and 3. As befits wind solutions, the velocities smoothly accelerate and cross a critical point where the velocity equals the isothermal gas sound speed (Bondi 1952; Parker 1958, 1965; Kato & Hachisu 1994). Crucially, up until day 11, this critical point is outside of the WD’s Roche radius (dotted lines in Figs. 2, 3, and

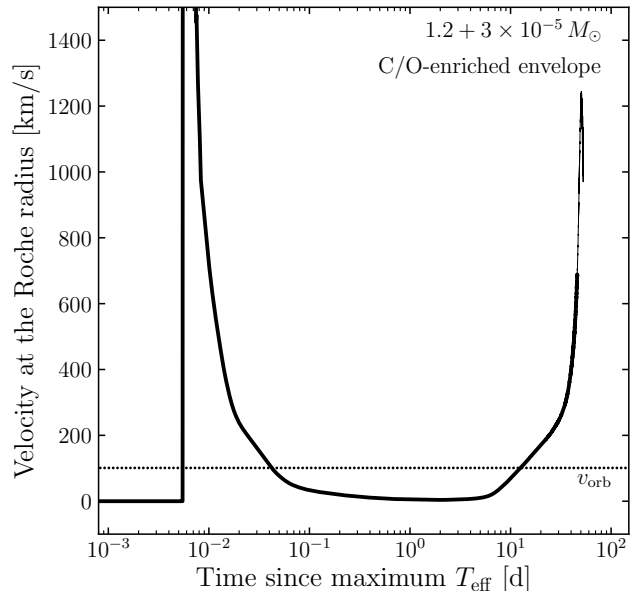


**Figure 6.** Time evolution of the velocity at the Roche radius for a  $1.2 M_{\odot}$  WD with a C/O-enriched  $3 \times 10^{-5} M_{\odot}$  outbursting envelope. The thin line represents the evolution after the photosphere recedes to the location of the iron opacity bump and is only shown for completeness, as our models are not quantitatively accurate during this phase. The Roche radius is calculated assuming a  $0.3 M_{\odot}$ ,  $0.3 R_{\odot}$  Roche-lobe-filling donor, and the dotted line is the WD’s orbital velocity in such a CV system.

5), assuming a  $0.3 M_{\odot}$ ,  $0.3 R_{\odot}$  Roche-lobe-filling companion, which we take as a typical donor in a classical nova system.<sup>3</sup> Since the envelopes are dominated by radiation pressure, the radii at which they become truly hydrodynamic, with velocities exceeding the radiation sound speed, are even farther out in the envelope and remain outside the Roche radius until day 37.

During the phase when the critical point is outside the Roche lobe, the velocity of material at the Roche radius remains low, only accelerating after it expands beyond this location. This can be seen in Figures 6 and 7, which show the velocity at the Roche radius,  $v_{\text{Roche}}$ , as a function of the time since reaching the maximum  $T_{\text{eff}}$  and the remaining envelope mass, respectively. The

<sup>3</sup> Most present-day CVs have periods below the period gap, implying donor masses  $\leq 0.2 M_{\odot}$  (Pala et al. 2022). However, this is a consequence of the deceleration in evolution as the donor mass decreases. The rate of novae is highest when the donor mass is highest because the accretion rate is at its maximum and the ignition mass is at its minimum. As a result, most of the novae during a CV’s evolution will occur shortly after birth, when the donor mass is highest. Thus, we use the mean of the pre-CV secondary mass distribution,  $0.3 M_{\odot}$  (Zorotovic et al. 2011), as our fiducial companion mass.

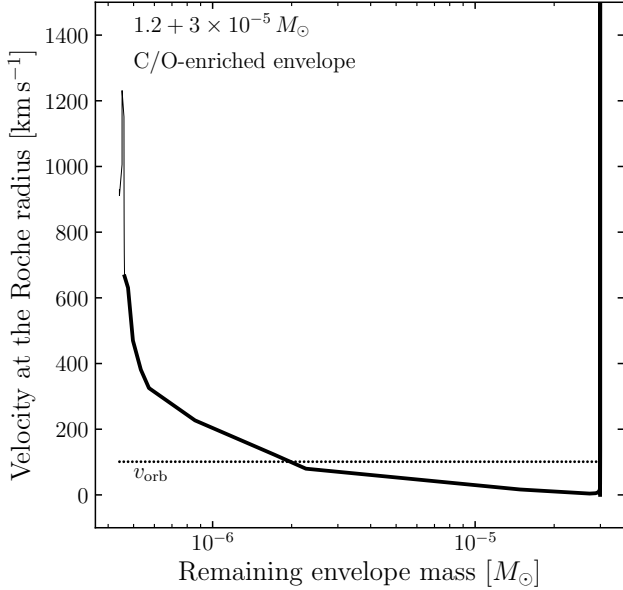


**Figure 7.** Same as Figure 6, but vs. the remaining envelope mass, defined as the mass contained between the maximum in the energy generation rate and the  $\tau = 2/3$  photosphere. Most of the mass is lost at low speeds for which the binary interaction cannot be neglected.

dotted lines are the WD’s orbital velocity in a CV with our assumed donor. After the initial burst of mass loss from surface  $\beta$ -decays, the velocity at the WD’s Roche radius drops below the WD’s orbital velocity,  $v_{\text{orb}}$ , and stays there until 11 d have passed, by which point more than 90% of the envelope mass has been ejected. The remaining envelope mass at the time when  $v_{\text{Roche}}$  increases to  $v_{\text{orb}}$  is given in column 5 of Table 1 for all of the models.

During this phase, the companion must play a crucial role in driving the outflow. When  $v_{\text{Roche}} \ll v_{\text{orb}}$ , the outflow will be analogous to standard Roche lobe overflow, with material attempting to leave the WD’s Roche lobe through the inner Lagrange point. However, the companion is overflowing its own Roche lobe and thus cannot accrete mass. Instead, the gradually outflowing material will expand into the circumbinary environment and make its way out of the  $L_2$  outer Lagrange point. From there, the torque from the binary will send the material out into the equatorial plane as a spiral wave, which shocks upon itself and forms an outflowing equatorial torus at  $\sim 10$  times the binary separation, similarly to mass outflows in non-degenerate contact binaries (Kuiper 1941; Shu et al. 1979; Pejcha 2014; Pejcha et al. 2016a,b, 2017).

For higher velocities up to  $\sim v_{\text{orb}}$ , the outflowing material is gravitationally focused by the companion into the equatorial plane in one or more outgoing spiral tails

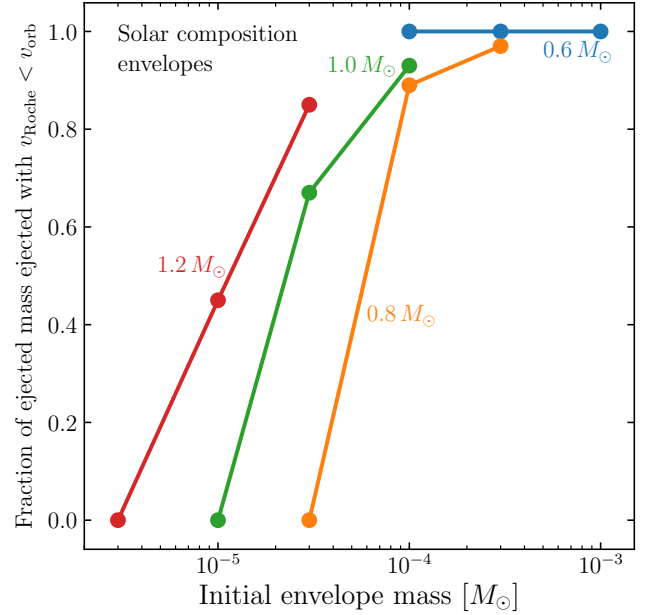


**Figure 8.** Fraction of the ejected mass that is ejected with  $v_{\text{Roche}} < v_{\text{orb}}$  vs. initial envelope mass for the solar composition envelope models. The WD masses are as labeled.

(Nagae et al. 2004; Jahanara et al. 2005; Liu et al. 2017; Saladino et al. 2018, 2019; MacLeod & Loeb 2020; Schröder et al. 2021). The morphology of this outflow will be somewhat different from the  $v_{\text{Roche}} \ll v_{\text{orb}}$  case, but the important points are that the outflow is equatorially focused, its speed is influenced by the binary interaction, and it carries away orbital angular momentum. The critical value of  $v_{\text{Roche}}/v_{\text{orb}}$  below which the binary shapes the outflow depends on the mass ratio, the wind profile, and other factors. Schröder et al. (2021) find a net decrease in the orbital separation due to the loss of angular momentum up to an ejection velocity of  $v_{\text{orb}}$  for a mass ratio of 1/3; for larger mass ratios (i.e., lower WD masses in the context of our study), mass loss leads to orbit shrinking up to even higher velocities of several times  $v_{\text{orb}}$ . To be conservative, we consider mass loss to be initiated and shaped by the binary up to a velocity of  $v_{\text{Roche}} = v_{\text{orb}}$  for all of our cases.

As the nova evolves and more of the envelope is lost, the acceleration region moves inwards and the velocity of the wind continues to increase. By day 37 for the  $1.2 + 3 \times 10^{-5} M_{\odot}$  C/O-enriched model, the iron opacity bump peaks at the WD’s Roche radius, and by day 45, the acceleration region has receded almost entirely within the Roche radius. It is likely that, by this point, a more spherical optically thick wind can successfully be launched since the wind reaches a velocity larger than the WD’s orbital velocity before crossing the Roche lobe. However, multi-dimensional radiation hydrody-

**Table 1.** Critical envelope masses and wind properties for the models presented in this work

WD mass [ $M_{\odot}$ ]	C/O enrichment?	Initial $M_{\text{env}}$ [ $M_{\odot}$ ]	Successful wind?	$M_{\text{env}}$ when $v_{\text{Roche}}$ rises above $v_{\text{orb}}$ <sup>a,b</sup> [ $M_{\odot}$ ]	$M_{\text{env}}$ when $\dot{M}_{\text{Roche}}$ falls below $10^{-7} M_{\odot} \text{ yr}^{-1}$ <sup>a</sup> [ $M_{\odot}$ ]	Percentage of ejected mass ejected with $v_{\text{Roche}} < v_{\text{orb}}$ <sup>c</sup>
0.6	No	$10^{-3}$	No	—	$5.8 \times 10^{-5}$	100%
0.6	No	$3 \times 10^{-4}$	No	—	$5.8 \times 10^{-5}$	100%
0.6	No	$10^{-4}$	No	—	$5.9 \times 10^{-5}$	100%
0.6	Yes	$10^{-3}$	Transitional	$2.1 \times 10^{-5}$	$1.9 \times 10^{-5}$	100%
0.6	Yes	$3 \times 10^{-4}$	Transitional	$2.5 \times 10^{-5}$	$2.0 \times 10^{-5}$	98%
0.6	Yes	$10^{-4}$	Transitional	$2.5 \times 10^{-5}$	$2.1 \times 10^{-5}$	95%
0.8	No	$3 \times 10^{-4}$	Transitional	$2.2 \times 10^{-5}$	$1.4 \times 10^{-5}$	97%
0.8	No	$10^{-4}$	Transitional	$2.3 \times 10^{-5}$	$1.4 \times 10^{-5}$	89%
0.8	No	$3 \times 10^{-5}$	Transitional	$3.0 \times 10^{-5}$	$1.4 \times 10^{-5}$	0%
0.8	Yes	$3 \times 10^{-4}$	Transitional	$9.2 \times 10^{-6}$	$6.4 \times 10^{-6}$	99%
0.8	Yes	$10^{-4}$	Transitional	$1.1 \times 10^{-5}$	$6.5 \times 10^{-6}$	95%
0.8	Yes	$3 \times 10^{-5}$	Yes	$1.2 \times 10^{-5}$	$6.6 \times 10^{-6}$	77%
0.8	Yes	$10^{-5}$	Yes	$1.0 \times 10^{-5}$	$6.5 \times 10^{-6}$	0%
1.0	No	$10^{-4}$	Transitional	$1.2 \times 10^{-5}$	$4.7 \times 10^{-6}$	93%
1.0	No	$3 \times 10^{-5}$	Yes	$1.3 \times 10^{-5}$	$4.7 \times 10^{-6}$	67%
1.0	No	$10^{-5}$	Yes	$1.0 \times 10^{-5}$	$5.0 \times 10^{-6}$	0%
1.0	Yes	$10^{-4}$	Yes	$4.6 \times 10^{-6}$	$2.2 \times 10^{-6}$	98%
1.0	Yes	$3 \times 10^{-5}$	Yes	$5.9 \times 10^{-6}$	$2.3 \times 10^{-6}$	87%
1.0	Yes	$10^{-5}$	Yes	$1.0 \times 10^{-5}$	$2.3 \times 10^{-6}$	0%
1.2	No	$3 \times 10^{-5}$	Yes	$5.5 \times 10^{-6}$	$1.1 \times 10^{-6}$	85%
1.2	No	$10^{-5}$	Yes	$6.0 \times 10^{-6}$	$1.2 \times 10^{-6}$	45%
1.2	No	$3 \times 10^{-6}$	Yes	$3.0 \times 10^{-6}$	$1.1 \times 10^{-6}$	0%
1.2	Yes	$3 \times 10^{-5}$	Yes	$2.0 \times 10^{-6}$	$4.6 \times 10^{-7}$	95%
1.2	Yes	$10^{-5}$	Yes	$2.6 \times 10^{-6}$	$4.9 \times 10^{-7}$	78%
1.2	Yes	$3 \times 10^{-6}$	Yes	$3.0 \times 10^{-6}$	$5.2 \times 10^{-7}$	0%

<sup>a</sup>For models with successful winds, the envelope mass is calculated as the mass between the location of the maximum burning rate and the  $\tau = 2/3$  photosphere. For transitional models and models with no winds, the outer envelope mass is measured at  $10 R_{\odot}$ .

<sup>b</sup>The brief initial phase when a small amount of mass is ejected at high velocities in some models due to  $\beta$ -decays near the surface is neglected in this column.

<sup>c</sup>We assume that any mass that reaches the Roche radius is successfully ejected, and that mass ejection ends when  $\dot{M}_{\text{Roche}}$  falls below  $10^{-7} M_{\odot} \text{ yr}^{-1}$ .

dynamic calculations are necessary to fully confirm this outcome. Crucially, this only occurs once the large majority of the envelope mass (94% for the C/O-enriched  $1.2 + 3 \times 10^{-5} M_{\odot}$  model) has been removed; prior to this point, the binary was primarily responsible for setting the properties of the ejected mass. This is also the case for most of the other models; see column 7 of Table 1 and Figures 8 and 9, which show the ratio of the mass ejected with  $v_{\text{Roche}} < v_{\text{orb}}$  to the total mass ejected. It is clear that standard optically thick winds are the main mechanism of mass loss only for the models with the lowest envelope masses we consider. These correspond to

systems with accretion rates of  $> 10^{-8} M_{\odot} \text{ yr}^{-1}$  (Yaron et al. 2005; Chomiuk et al. 2021), which yield recurrent novae (Hachisu & Kato 2001; Schaefer 2010) but are a small minority of CVs (Pala et al. 2022).

The  $\tau = 2/3$  photosphere, shown as circles in Figures 2, 3, and 5, continues to move inwards in radius with time, to the point that the iron opacity bump is outside the photosphere during the final phases of the simulations with successfully launched outflows. By default, MESA does not differentiate between radiation effects in optically thick and optically thin regions. For instance, it is assumed that the radiation and matter are always



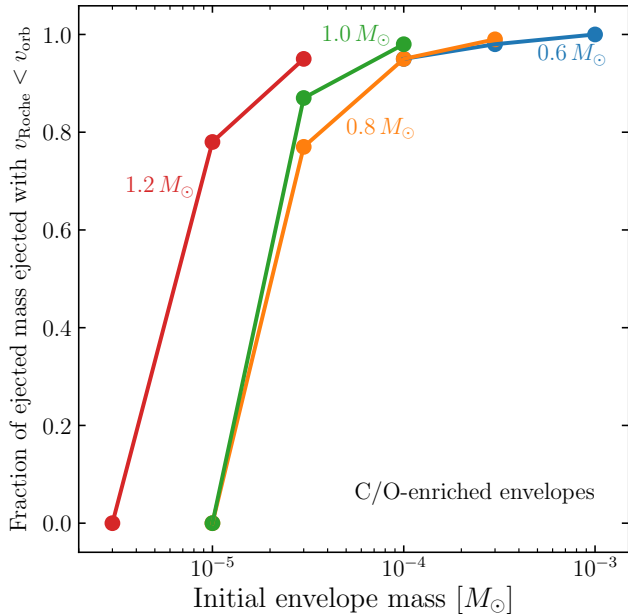


**Figure 9.** Same as Fig. 8, but for the C/O-enriched models.

in thermal equilibrium, so that the radiation pressure is only a function of temperature. As a result, the velocity profile found by MESA continues to accelerate through the iron opacity bump even when the material is optically thin. Physically, the low optical depth should imply a low interaction probability between photons and envelope material, reducing the radiative acceleration. However, this will be mitigated by line-broadening due to the velocity gradient, which will increase the opacity from the zero-velocity Rosseland mean value used here (Castor et al. 1975). A complete physical description of wind acceleration in this regime necessitates a hydrodynamical radiative transfer calculation to account for these effects, ideally in multiple dimensions to allow for clumping and porosity (Paczynski 1969; Shaviv 2001; Owocki et al. 2004; Jiang et al. 2015) and including non-local thermodynamic equilibrium effects (Hauschildt et al. 1995, 1996, 1997). This is outside the scope of the present work and will be the subject of future study.

While the lack of self-consistency renders the calculations untrustworthy during this stage, it is important to note that this phase only occurs near the end of the simulations. Figure 10 shows that the mass outflow rate declines precipitously as the remaining envelope mass approaches the maximum allowed mass for a steadily burning, thermally stable hydrostatic envelope, marking the end of the mass outflow stage of the nova outburst. (The remaining envelope masses for our models when the mass outflow rate at the Roche radius,  $\dot{M}_{\text{Roche}}$ ,

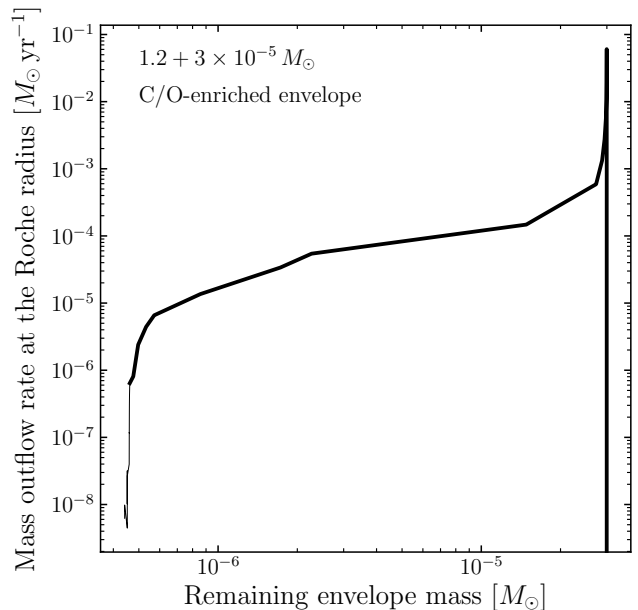


**Figure 10.** Mass outflow rate at the Roche radius vs. the remaining envelope mass for the  $1.2 + 3 \times 10^{-5} M_{\odot}$  C/O-enriched envelope model. The thin line represents the evolution after the photosphere recedes to the iron opacity bump when a more accurate radiation transport calculation for the wind is needed.

drops below  $10^{-7} M_{\odot} \text{ yr}^{-1}$  are listed in column 6 of Table 1.) It is during this sharp drop in mass outflow rate at the end of the nova wind phase, after almost all of the mass has been ejected, that the photosphere recedes within the iron opacity bump, as shown by the thin lines in Figure 6, 7, and 10. Thus, even though the MESA calculation is not self-consistent near the end of the outburst, most of the simulation takes place while the acceleration region is below the photosphere. Our main conclusion that binary interaction causes most of the mass loss is therefore robust.

Simulations that launch optically thick winds that become completely unbound are shown as filled red and blue circles in Figure 11. The red solid and blue dotted lines show the envelope masses for the labeled compositions at which the mass outflow rates decline sharply, marking the end of the mass loss phase for models with successful winds. Higher WD masses, lower envelope masses, and more C/O enrichment all help to launch optically thick winds in isolation. However, not all simulations are able to successfully form winds. We discuss these other outcomes in the following subsections.

### 3.2. Models with no winds

In sharp contrast to our simulations with successful optically thick winds, the  $0.6 M_{\odot}$  models with solar com-

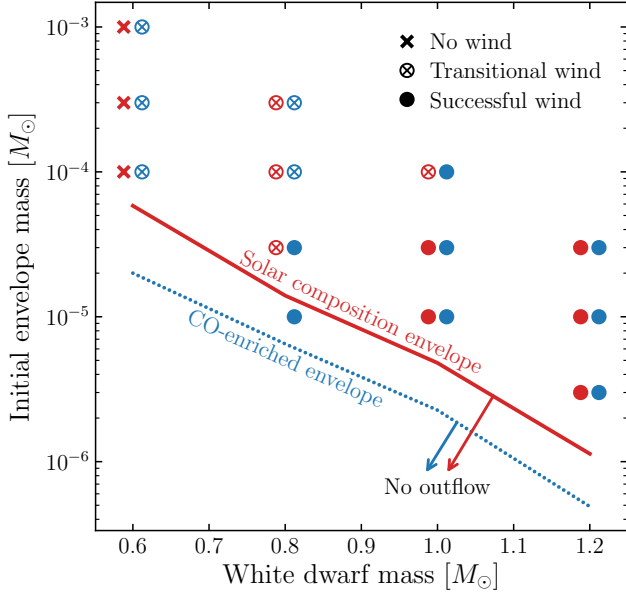


**Figure 11.** Outcomes of outbursts for given initial envelope mass vs. WD mass, as labeled. Red points shifted slightly to the left of their actual WD masses denote models with solar composition envelopes; blue points to the right of their WD masses are models with CO-enriched envelopes. The solid and dotted lines mark the approximate envelope mass below which thin, steady-state, thermally stable hydrostatic envelope solutions exist and outflows cease.

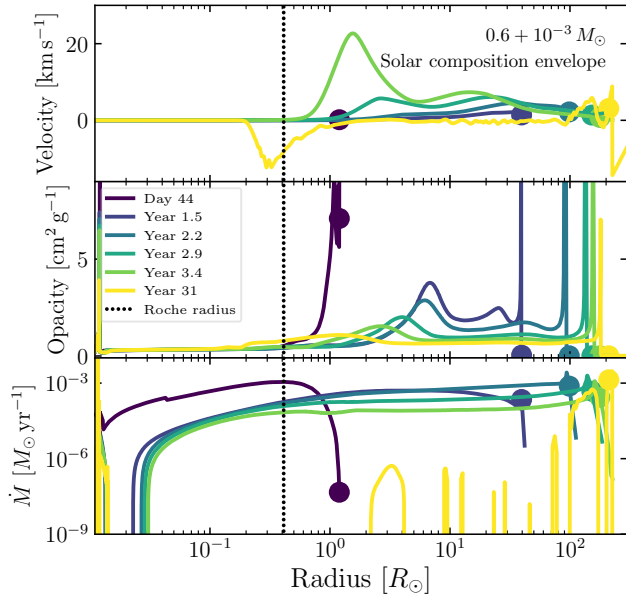


**Figure 12.** Same as Fig. 2, but for the  $0.6 + 10^{-3} M_{\odot}$  solar composition envelope model. Note the changes in axes and times.

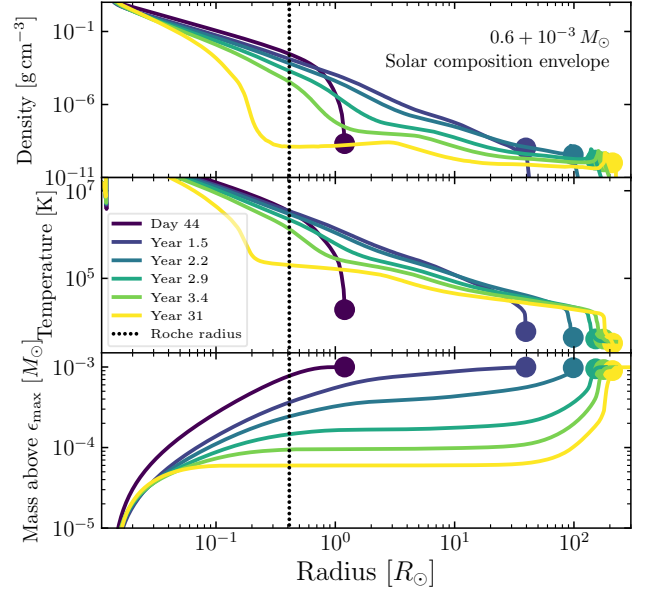


**Figure 13.** Same as Fig. 3, but for the  $0.6 + 10^{-3} M_{\odot}$  solar composition envelope model. Note the changes in axes and times.

position envelopes, shown as red Xs in Figure 11, never launch steady-state outflows. These envelopes remain completely gravitationally bound for their entire evolution, with velocities that never approach the sound speed or the escape speed. Radial profiles at various times during the evolution of the  $0.6 + 10^{-3} M_{\odot}$  solar composition envelope simulation are shown in Figures 12 and 13. The lack of a steady state wind is readily apparent in the top panel of Figure 12, which shows that the velocities remain in the tens of  $\text{km s}^{-1}$  within the envelope and asymptote to zero at the photosphere. By the end of the simulation, 31 yr after the beginning of the calculation, the mass flux throughout the envelope has dropped to nearly zero with small spikes due to weak shocks in the outer envelope. The envelope is now in a steady state similar to a red giant branch star: an expanded, hydrostatic envelope burning hydrogen at its base, surrounding a degenerate core. If such an outbursting WD were in a CV, the companion would necessarily drive off most of the envelope, leaving only a small remnant mass equal to the maximum mass for a thin, hydrostatic, thermally stable envelope solution.

### 3.3. Transitional models

Some simulations launch an optically thick wind that remains enclosed by a layer of outer material that is too massive to accelerate. As a result, the envelope is never completely unbound: the material at large radii stops the progress of the wind. Eventually, the wind is completely choked, and all of the material falls below the

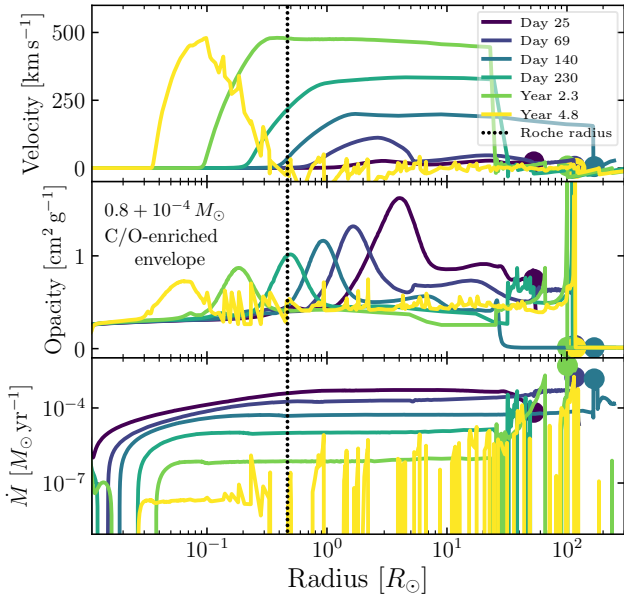


**Figure 14.** Same as Fig. 2, but for the  $0.8 + 10^{-4} M_{\odot}$  C/O-enriched envelope model. Note the changes in axes and times.

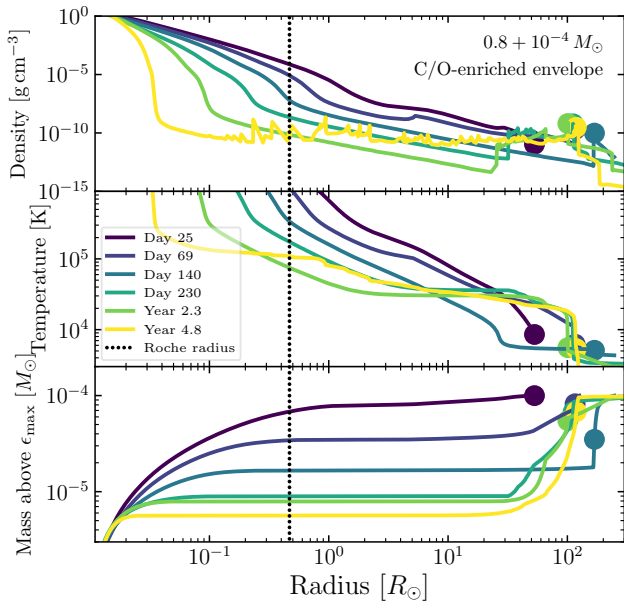


**Figure 15.** Same as Fig. 3, but for the  $0.8 + 10^{-4} M_{\odot}$  C/O-enriched envelope model. Note the changes in axes and times.

local escape speed from the WD. We call these “transitional” cases, shown as combined Xs and open circles in Figure 11.

Figures 14 and 15 show radial profiles of the  $0.8 + 10^{-4} M_{\odot}$ , C/O-enriched envelope model, which is an example of a transitional case. As seen in the top panel

of Figure 14, a steady-state optically thick wind in the inner regions develops by day 140, but the mass profile shown in the bottom panel of Figure 15 demonstrates that most of the outer envelope mass remains at low velocities. This bound mass at the surface of the envelope blocks the outflow, preventing the formation of a successful wind. After 3.6 yr have passed, the wind collapses into a breeze configuration (Parker 1965) similar to the profile shown at year 4.8.

It is likely that if the companion were taken into account, binary interaction would remove enough of the outer material in the early phase of the outburst to allow for the successful formation of a completely unbound wind during the later stages of mass loss. As with the previous outcomes, it remains the case that most of the mass ejection would be initiated by the binary interaction and not by an isotropic optically thick wind; see column 5 of Table 1 and Figures 8 and 9.

#### 4. COMPARISON TO PREVIOUS WORK

In this section, we compare the results of our numerical hydrodynamic calculations to previous analytic and numeric work on nova outbursts.

Kato & Hachisu (1994)’s frequently cited analytic study of optically thick winds has formed the basis for our theoretical understanding of classical nova outflows for almost 30 years. They integrate the standard wind equations (e.g., Bondi 1952 and Parker 1958, 1965) inwards and outwards from the sonic point to generate time-independent envelope solutions in which winds are accelerated off of the iron opacity bump. Our numerical time-dependent envelope profiles and relations such as the mass outflow rate and asymptotic velocity as a function of the envelope mass broadly agree with their analytic solutions, although quantitative comparisons are difficult due to the differences in our envelope compositions.

In their more recent work (Kato & Hachisu 2009), they perform some calculations with solar composition envelopes, which we can directly compare to our results. In their Figure 10, we see that the boundaries for envelope masses that successfully launch winds vs. those that instead adopt “breeze” solutions are shifted compared to our findings, which are summarized in Figure 11: they find successful winds for WDs as low-mass as  $\simeq 0.5 M_{\odot}$ , while our solar composition simulations only launch successful winds for masses  $\gtrsim 0.8 M_{\odot}$ , with transitional or failed winds below this mass.

The most obvious difference between our methodologies is their use of time-independent, steady-state solutions vs. our time-dependent simulations. This is particularly obvious during the early stages of evolution, as the

envelope expands and readjusts towards its steady state wind profile. For example, the excess mass at large radii that ultimately halts the wind in our transitional models will not be captured in their time-independent calculations. This is likely the reason for our disagreement regarding the success of winds for lower-mass WDs.

Prialnik & Kovetz (1995) and Yaron et al. (2005), and works that build off of these two studies such as Epelstein et al. (2007) and Hillman et al. (2014, 2016), present a large suite of time-dependent nova models, with a range of accretion rates onto WDs of a variety of masses and core temperatures. Because our work sets the convective envelope masses by hand to avoid the complications of the pre-outburst accretion, diffusion, and mixing, none of the parameters at the onset of the outbursts described in our two sets of studies match exactly. Still, some models provide a qualitative and informative comparison.

Each of Prialnik & Kovetz (1995) and Yaron et al. (2005)'s  $0.65 M_{\odot}$ ,  $10^{-8} M_{\odot} \text{ yr}^{-1}$  models results in a convective envelope mass of  $\sim 10^{-4} M_{\odot}$  with  $Z \sim 0.02$ , similar to our  $0.6 + 10^{-4} M_{\odot}$  solar metallicity models. However, they find that these envelopes are ejected from the binary, albeit at low velocities  $\sim 130 \text{ km s}^{-1}$ , whereas none of our  $0.6 M_{\odot}$  models successfully launches a sustained wind. The disagreement is even more stark for their cold (core temperature of  $10^7 \text{ K}$ )  $0.65 M_{\odot}$ ,  $10^{-10}$  and  $10^{-11} M_{\odot} \text{ yr}^{-1}$  models, which yield convective envelope masses of  $2.4 - 2.8 \times 10^{-4} M_{\odot}$  with  $Z = 0.1 - 0.2$ , roughly similar to our C/O-enriched  $0.6 + 3 \times 10^{-4} M_{\odot}$  model. They find that these models yield ejected envelopes with an average velocity of  $600 - 2700 \text{ km s}^{-1}$ , in direct contrast with the gravitationally bound envelopes exhibited by our models. In fact, Prialnik & Kovetz (1995), Yaron et al. (2005), and Shen et al. (2009), which all use the same code, found mass ejection during nova outbursts for WDs as low in mass as  $0.4 M_{\odot}$ , in clear contrast with the present work and the analytic work of Kato & Hachisu (2009).

Yaron et al. (2005)'s cold  $1.0 M_{\odot}$ ,  $10^{-11} M_{\odot} \text{ yr}^{-1}$  model results in an ejected envelope of  $10^{-4} M_{\odot}$  with  $Z = 0.2$ , with an average ejection velocity of  $1100 \text{ km s}^{-1}$ , which is not too dissimilar from the outcome for our  $1.0 + 10^{-4} M_{\odot}$  C/O-enriched model. However, the timescale over which this is achieved differs drastically between our two studies: Yaron et al. (2005) find a mass-loss phase that lasts for 35 d, whereas we find that mass loss persists for almost a factor of 10 longer.

One possibility for these discrepancies is Prialnik & Kovetz (1995) and Yaron et al. (2005)'s mass loss criteria: once the velocity in a subsurface region in their

simulations becomes supersonic and has a positive velocity gradient, mass is removed from the outer cell at the subsurface zone's rate of  $\dot{M} = 4\pi r^2 v$ . However, it is not obvious that this subsurface mass flux is the correct value for the surface mass loss rate, particularly during the initial phase of the outburst, when the mass flux is not constant throughout the envelope. Moreover, in our transitional models, an optically thick wind is launched but ultimately remains bound; Prialnik & Kovetz (1995) and Yaron et al. (2005)'s mass loss algorithm may erroneously remove this mass. Still, without an in-depth code comparison, it is difficult to pinpoint the ultimate reason(s) for the differences between our results and those of Prialnik & Kovetz (1995) and Yaron et al. (2005); such a comparison would be a useful future endeavor.

The NOVA code has a long and rich history of studies of classical nova outbursts (e.g., Kutter & Sparks 1972; Politano et al. 1995; Starrfield et al. 1998, 2000, 2009, 2016). In the most recent work to use the NOVA code, Starrfield et al. (2020) perform a suite of simulations of WDs of a range of masses accreting material with a variety of accretion rates and compositions. The best matches with our models are for their simulations with solar composition envelopes and 25% WD, 75% solar composition envelopes. In direct contrast with our results, and those of Kato & Hachisu (1994), Prialnik & Kovetz (1995), Yaron et al. (2005), and others, Starrfield et al. (2020) find that very little mass is ejected for these compositions. Essentially no mass is ejected for their solar composition envelopes, and  $\leq 5\%$  of the nova envelope is ejected for their 25% WD, 75% solar composition envelopes for WD masses  $\leq 1.0 M_{\odot}$ . Their higher mass models do eject tens of percent of their envelopes, but these ejected masses are still much less than the 98% ejected fraction that we find for our C/O-enriched,  $1.2 + 3 \times 10^{-5} M_{\odot}$  model, which provides the closest match.

The reason for their low ejected masses likely lies in the stopping criterion employed by Starrfield et al. (2020). Once mass expands to radii of a few times  $10^{12} \text{ cm}$ , their simulations are ended due to the material reaching densities below the lower bounds of their equation of state and opacity tables. However, this condition is reached very early in the evolution of our simulations. If we were to employ a similar condition, we would also find very low ejected masses simply because most of the mass ejection occurs after the outermost zones reach these radii. This extended material can also fall off of our equation of state and opacity tables, but since the material is at extremely low optical depths, any uncertainties are inconsequential for the evolution

of the bulk of the envelope. Thus, we regard [Starrfield et al. \(2020\)](#)'s findings of very low ejected masses to be a consequence of premature stopping conditions, and we encourage them to extend their simulations to later times.

Our study is certainly not the first theoretical work to examine the role that a companion may play in driving mass loss during novae (e.g., [MacDonald 1980](#); [MacDonald et al. 1985](#); [MacDonald 1986](#); [Kato & Hachisu 1994](#), [2011](#)). However, these previous studies only consider the companion's impact on one-dimensional spherically symmetric steady-state envelope solutions. They do not allow for the possibility that the companion entirely disrupts the standard spherical wind solution and instead shapes the mass loss into an equatorial outflow. We have shown that the latter case is more likely at most times for most nova systems.

[Livio et al. \(1990\)](#) infer that the donor star is important for shaping, and perhaps even driving, mass loss in classical novae due to the empirical observation that the pseudo-photosphere is located at a radius well outside of the binary separation. However, even given this hierarchy of radii, the companion would still not dominate the outflow properties if the outflow were ejected from the WD's surface at a velocity much faster than the orbital velocity. In the present study, we show that the outflow velocities at the Roche radius are in fact slower than the orbital velocity during the majority of the mass loss phase for most novae, and thus the companion does play a dominant role in driving mass loss during outbursts.

[Livio et al. \(1990\)](#) also perform a two-dimensional axisymmetric hydrodynamic simulation of a slow WD wind that is focused onto the equatorial plane by the companion, which is approximated as a smeared-out axisymmetric ring. In reality, the three-dimensional configuration of the CV will instead likely result in an ejected spiral that self-shocks and develops into an outflow driven by the binary torque ([Pejcha et al. 2016a,b](#); [Schröder et al. 2021](#)).

## 5. CONCLUSIONS

In this paper, we have described our suite of hydrodynamic stellar evolution simulations of isolated WDs undergoing classical nova eruptions. We have shown that, for typical systems, most of the mass that is lost in optically thick winds reaches the WD's Roche radius at velocities lower than the orbital velocity. As a result, when the binary companion is taken into account, the properties of mass driven from the system will actually be primarily set by the binary interaction. This is even more true for lower-mass WDs  $\lesssim 0.8 M_{\odot}$ , for which no optically thick winds are successfully launched in isola-

tion; for these systems, mass loss would not occur at all if not for the binary interaction. Any study aiming to predict classical nova observables, from optical light curves and spectra to non-thermal shock signatures, needs to account for the dominating influence of the binary companion on the outflows. The only CVs for which optically thick winds drive the majority of mass loss are the rare systems with high accretion rates  $> 10^{-8} M_{\odot} \text{ yr}^{-1}$ , which yield the lowest envelope ignition masses.

Our results predict that much of the outflowing mass in classical novae is likely to be focused into the equatorial plane in the form of spiral arms that may undergo internal shocks and dissipate and radiate some fraction of their kinetic energy, as seen in analogous simulations of mass loss in contact binaries and high-mass X-ray binaries ([Pejcha et al. 2016a,b](#); [Schröder et al. 2021](#)). However, these studies differ in important ways from the classical nova case, so quantitative predictions of the geometry and observables associated with this binary-induced mass loss await future dedicated multi-dimensional radiation hydrodynamical simulations.

The self-collision of the spiral arms, together with the subsequent shocks between late-time high-speed radiation-pressure-driven winds and earlier-time slower binary-driven mass loss, are plausibly responsible for the rich and complex light curves of classical novae, including the evidence for shock-generated hard X-rays and non-thermal gamma-rays (e.g., [Chomiuk et al. 2021](#)). The key role of the binary in driving nova winds might also explain the super-Eddington luminosities observed for some classical novae. These super-Eddington luminosities cannot be understood using radiation-pressure-driven winds alone but may be explained by the additional kinetic energy gained through interaction with the binary.

For novae in symbiotic systems (e.g., [Mikołajewska 2010](#)), which have giant companions and thus much larger binary separations, the acceleration of the outflows from the WD will not be affected by the binary interaction. However, even in these systems, the influence of the companion on the nova observables cannot be neglected. The companion's wind will both reprocess the resulting radiation as well as lead to shock interaction with the nova outflow.

The orbital energy and angular momentum carried away by the binary-driven mass loss will have a profound effect on the long-term evolution of the CV, possibly destabilizing the binary enough to cause a merger ([Shen 2015](#); [Metzger et al. 2021](#)). This is especially true for CVs with lower-mass WDs, since the mass ratio is higher and because the nova ignition masses are larger, which means each nova event has more of an effect on



the post-nova binary parameters. This preferential destruction of CVs with lower-mass WDs would explain the large discrepancy between the CV mass distribution and that of field WDs and pre-CVs (Zorotovic et al. 2011; Nelemans et al. 2016; Schreiber et al. 2016; Pala et al. 2020, 2022) and will be the subject of future studies.

Future work will also include multi-dimensional radiation hydrodynamics calculations to better quantify the transition between a binary-dominated outflow and the successful launching of a more spherical optically thick wind as well as hydrodynamic simulations of the interaction between these two modes of mass ejection. Such studies will be necessary for a complete understanding of the surprisingly complex physics of classical novae and will have a broad applicability to investigations of mass

loss in other contexts, such as contact binaries, common envelope systems, and high-mass X-ray binaries.

*Software:* `matplotlib` (Hunter 2007), `MESA` (Paxton et al. 2011, 2013, 2015, 2018)

We thank Laura Chomiuk, Dan Kasen, Brian Metzger, Raffaella Margutti, Alison Miller, Joe Patterson, Ondřej Pejcha, Brad Schaefer, and Jenő Sokoloski for helpful discussions, Bill Paxton and the MESA Council for developing `MESA`, and the referee for their thoughtful review. This work was supported by NASA through the Astrophysics Theory Program (80NSSC20K0544) and by the Research Corporation for Science Advancement through a “Scialog: Time Domain Astrophysics” award. This research used the Savio computational cluster resource provided by the Berkeley Research Computing program at the University of California, Berkeley (supported by the UC Berkeley Chancellor, Vice Chancellor of Research, and Office of the CIO).

## APPENDIX

The hydrodynamic `MESA` calculations presented in this work are informed by previous studies that used `MESA` to simulate hydrodynamical outflows (Quataert et al. 2016; Fuller 2017; Shen & Schwab 2017). These studies helped to define the necessary flags and parameters to set in the `inlist`, which we display below, to allow for the development of outflowing winds.

In addition to these flags, we also implement several additional modifications for our particular set of simulations. In the initial stages of the outburst as the envelope is being accelerated to a steady wind solution, the outermost zone can have issues converging to a solution. To circumvent this roadblock, we restrict each cell’s mass to be at least  $10^{-12}$  of the enclosed mass at that coordinate until the photosphere reaches  $1 R_{\odot}$ . After this point, the minimum cell mass is reduced to  $10^{-99}$  of the enclosed mass at that coordinate; i.e., cells are allowed to become as small as necessary, ensuring the simulation is not starved for gridpoints.

Once the outflow has begun, an opacity minimum of  $0.01 \text{ cm}^2 \text{ g}^{-1}$  is established in the optically thin region above the photosphere to increase numerical stability. For some models that encounter numerical difficulties, the opacity in this region is later further constrained to be a constant  $0.01 \text{ cm}^2 \text{ g}^{-1}$ .

`&star_job`

```
! initialize the model
load_saved_model = .true.
saved_model_name = '1.0.2e7_1e-4_0.2.mod'
set_initial_age = .true.
initial_age = 0
set_initial_model_number = .true.
initial_model_number = 0

! set the outer optical depth to be  $0.01 \times 2/3$ 
set_to_this_tau_factor = 1e-2
set_tau_factor = .true.

! set the nuclear network
change_net = .true.
```

```

new_net_name = 'cno_extras.net'

! turn on hydrodynamics
change_v_flag = .true.
new_v_flag = .true.

/ ! end of star_job namelist

&controls

min_dq = 1d-99 ! 1d-12 until photosphere reaches 1 Rsol, then switch to 1d-99
logQ_min_limit = -99
min_timestep_limit = 1d-99
use_Ledoux_criterion = .true.

! set outer boundary conditions for hydrodynamics
use_momentum_outer_BC = .true.
use_compression_outer_BC = .true.
use_zero_Pgas_outer_BC = .true.

! limit convective velocity and acceleration
max_conv_vel_div_csound = 1d0
mlt_accel_g_theta = 1
min_T_for_acceleration_limited_conv_velocity = 0

! turn on artificial viscosity
use_artificial_viscosity = .true.

! use Type 2 opacities to account for C/O enrichment
use_Type2_opacities = .true.
Zbase = 0.02

merge_if_dlnR_too_small = .true. ! turned on near the end of some runs to stabilize shocks
mesh_min_dlnR = 1d-7

use_other_kap = .true. ! set an opacity floor for optically thin material

/ ! end of controls namelist

```

## REFERENCES

- Ackermann, M., Ajello, M., Albert, A., et al. 2014, *Science*, 345, 554, doi: [10.1126/science.1253947](https://doi.org/10.1126/science.1253947)
- Alexakis, A., Calder, A. C., Heger, A., et al. 2004, *ApJ*, 602, 931, doi: [10.1086/381086](https://doi.org/10.1086/381086)
- Asplund, M., Grevesse, N., Sauval, A. J., & Scott, P. 2009, *ARA&A*, 47, 481, doi: [10.1146/annurev.astro.46.060407.145222](https://doi.org/10.1146/annurev.astro.46.060407.145222)
- Aydi, E., Page, K. L., Kuin, N. P. M., et al. 2018, *MNRAS*, 474, 2679, doi: [10.1093/mnras/stx2678](https://doi.org/10.1093/mnras/stx2678)
- Aydi, E., Chomiuk, L., Izzo, L., et al. 2020a, *ApJ*, 905, 62, doi: [10.3847/1538-4357/abc3bb](https://doi.org/10.3847/1538-4357/abc3bb)
- Aydi, E., Sokolovsky, K. V., Chomiuk, L., et al. 2020b, *Nature Astronomy*, 4, 776, doi: [10.1038/s41550-020-1070-y](https://doi.org/10.1038/s41550-020-1070-y)
- Bode, M. F., & Evans, A. 2008, *Classical Novae* (2nd ed.; Cambridge: Cambridge University Press)
- Bondi, H. 1952, *MNRAS*, 112, 195, doi: [10.1093/mnras/112.2.195](https://doi.org/10.1093/mnras/112.2.195)

- Cao, Y., Kasliwal, M. M., Neill, J. D., et al. 2012, *ApJ*, 752, 133, doi: [10.1088/0004-637X/752/2/133](https://doi.org/10.1088/0004-637X/752/2/133)
- Casanova, J., José, J., García-Berro, E., Calder, A., & Shore, S. N. 2010, *A&A*, 513, L5, doi: [10.1051/0004-6361/201014178](https://doi.org/10.1051/0004-6361/201014178)
- . 2011a, *A&A*, 527, A5, doi: [10.1051/0004-6361/201015895](https://doi.org/10.1051/0004-6361/201015895)
- Casanova, J., José, J., García-Berro, E., & Shore, S. N. 2016, *A&A*, 595, A28, doi: [10.1051/0004-6361/201628707](https://doi.org/10.1051/0004-6361/201628707)
- Casanova, J., José, J., García-Berro, E., Shore, S. N., & Calder, A. C. 2011b, *Nature*, 478, 490, doi: [10.1038/nature10520](https://doi.org/10.1038/nature10520)
- Casanova, J., José, J., & Shore, S. N. 2018, *A&A*, 619, A121, doi: [10.1051/0004-6361/201833422](https://doi.org/10.1051/0004-6361/201833422)
- Castor, J. I., Abbott, D. C., & Klein, R. I. 1975, *ApJ*, 195, 157, doi: [10.1086/153315](https://doi.org/10.1086/153315)
- Chen, H.-L., Woods, T. E., Yungelson, L. R., et al. 2019, *MNRAS*, 490, 1678, doi: [10.1093/mnras/stz2644](https://doi.org/10.1093/mnras/stz2644)
- Chomiuk, L., Metzger, B. D., & Shen, K. J. 2021, *ARA&A*, 59, doi: [10.1146/annurev-astro-112420-114502](https://doi.org/10.1146/annurev-astro-112420-114502)
- Chomiuk, L., Linford, J. D., Yang, J., et al. 2014, *Nature*, 514, 339, doi: [10.1038/nature13773](https://doi.org/10.1038/nature13773)
- Cyburt, R. H., Amthor, A. M., Ferguson, R., et al. 2010, *ApJS*, 189, 240, doi: [10.1088/0067-0049/189/1/240](https://doi.org/10.1088/0067-0049/189/1/240)
- Denissenkov, P. A., Herwig, F., Bildsten, L., & Paxton, B. 2013, *ApJ*, 762, 8, doi: [10.1088/0004-637X/762/1/8](https://doi.org/10.1088/0004-637X/762/1/8)
- Denissenkov, P. A., Truran, J. W., Pignatari, M., et al. 2014, *MNRAS*, 442, 2058, doi: [10.1093/mnras/stu1000](https://doi.org/10.1093/mnras/stu1000)
- Epelstein, N., Yaron, O., Kovetz, A., & Prialnik, D. 2007, *MNRAS*, 374, 1449, doi: [10.1111/j.1365-2966.2006.11254.x](https://doi.org/10.1111/j.1365-2966.2006.11254.x)
- Finzell, T., Chomiuk, L., Metzger, B. D., et al. 2018, *ApJ*, 852, 108, doi: [10.3847/1538-4357/aaa12a](https://doi.org/10.3847/1538-4357/aaa12a)
- Fujimoto, M. Y. 1982, *ApJ*, 257, 767, doi: [10.1086/160030](https://doi.org/10.1086/160030)
- Fuller, J. 2017, *MNRAS*, 470, 1642, doi: [10.1093/mnras/stx1314](https://doi.org/10.1093/mnras/stx1314)
- Gehrz, R. D., Truran, J. W., Williams, R. E., & Starrfield, S. 1998, *PASP*, 110, 3, doi: [10.1086/316107](https://doi.org/10.1086/316107)
- Ginzburg, S., & Quataert, E. 2021, *MNRAS*, 507, 475, doi: [10.1093/mnras/stab2170](https://doi.org/10.1093/mnras/stab2170)
- Glasner, S. A., & Livne, E. 1995, *ApJL*, 445, L149, doi: [10.1086/187911](https://doi.org/10.1086/187911)
- Glasner, S. A., Livne, E., & Truran, J. W. 1997, *ApJ*, 475, 754, doi: [10.1086/303561](https://doi.org/10.1086/303561)
- . 2012, *MNRAS*, 427, 2411, doi: [10.1111/j.1365-2966.2012.22103.x](https://doi.org/10.1111/j.1365-2966.2012.22103.x)
- Guo, Y., Wu, C., & Wang, B. 2022, *A&A*, 660, A53, doi: [10.1051/0004-6361/202142163](https://doi.org/10.1051/0004-6361/202142163)
- Hachisu, I., & Kato, M. 2001, *ApJ*, 558, 323, doi: [10.1086/321601](https://doi.org/10.1086/321601)
- Hauschildt, P. H., Baron, E., Starrfield, S., & Allard, F. 1996, *ApJ*, 462, 386, doi: [10.1086/177160](https://doi.org/10.1086/177160)
- Hauschildt, P. H., Shore, S. N., Schwarz, G. J., et al. 1997, *ApJ*, 490, 803
- Hauschildt, P. H., Starrfield, S., Shore, S. N., Allard, F., & Baron, E. 1995, *ApJ*, 447, 829, doi: [10.1086/175921](https://doi.org/10.1086/175921)
- Hillman, Y., & Gerbi, M. 2022, *MNRAS*, 511, 5570, doi: [10.1093/mnras/stac432](https://doi.org/10.1093/mnras/stac432)
- Hillman, Y., Prialnik, D., Kovetz, A., & Shara, M. M. 2016, *ApJ*, 819, 168, doi: [10.3847/0004-637X/819/2/168](https://doi.org/10.3847/0004-637X/819/2/168)
- Hillman, Y., Prialnik, D., Kovetz, A., Shara, M. M., & Neill, J. D. 2014, *MNRAS*, 437, 1962, doi: [10.1093/mnras/stt2027](https://doi.org/10.1093/mnras/stt2027)
- Hunter, J. D. 2007, *Computing in Science & Engineering*, 9, 90, doi: [10.1109/MCSE.2007.55](https://doi.org/10.1109/MCSE.2007.55)
- Iglesias, C. A., Rogers, F. J., & Wilson, B. G. 1990, *ApJ*, 360, 221, doi: [10.1086/169110](https://doi.org/10.1086/169110)
- Jahanara, B., Mitsumoto, M., Oka, K., et al. 2005, *A&A*, 441, 589, doi: [10.1051/0004-6361:20052828](https://doi.org/10.1051/0004-6361:20052828)
- Jiang, Y.-F., Cantiello, M., Bildsten, L., Quataert, E., & Blaes, O. 2015, *ApJ*, 813, 74, doi: [10.1088/0004-637X/813/1/74](https://doi.org/10.1088/0004-637X/813/1/74)
- José, J., & Hernanz, M. 2007, *Journal of Physics G Nuclear Physics*, 34, 431, doi: [10.1088/0954-3899/34/12/R01](https://doi.org/10.1088/0954-3899/34/12/R01)
- Kato, M., & Hachisu, I. 1994, *ApJ*, 437, 802, doi: [10.1086/175041](https://doi.org/10.1086/175041)
- . 2009, *ApJ*, 699, 1293, doi: [10.1088/0004-637X/699/2/1293](https://doi.org/10.1088/0004-637X/699/2/1293)
- . 2011, *ApJ*, 743, 157, doi: [10.1088/0004-637X/743/2/157](https://doi.org/10.1088/0004-637X/743/2/157)
- Kemp, A. J., Karakas, A. I., Casey, A. R., Kobayashi, C., & Izzard, R. G. 2022, *MNRAS*, 509, 1175, doi: [10.1093/mnras/stab3103](https://doi.org/10.1093/mnras/stab3103)
- Kippenhahn, R., & Thomas, H. 1978, *A&A*, 63, 265
- König, O., Wilms, J., Arcodia, R., et al. 2022, *Nature*, 605, 248, doi: [10.1038/s41586-022-04635-y](https://doi.org/10.1038/s41586-022-04635-y)
- Kovetz, A., & Prialnik, D. 1985, *ApJ*, 291, 812, doi: [10.1086/163117](https://doi.org/10.1086/163117)
- Kuiper, G. P. 1941, *ApJ*, 93, 133, doi: [10.1086/144252](https://doi.org/10.1086/144252)
- Kutter, G. S., & Sparks, W. M. 1972, *ApJ*, 175, 407, doi: [10.1086/151567](https://doi.org/10.1086/151567)
- . 1989, *ApJ*, 340, 985, doi: [10.1086/167452](https://doi.org/10.1086/167452)
- Lemut, A., Bemmerer, D., Confortola, F., et al. 2006, *Physics Letters B*, 634, 483, doi: [10.1016/j.physletb.2006.02.021](https://doi.org/10.1016/j.physletb.2006.02.021)
- Leung, S.-C., & Siebert, T. 2021, *MNRAS*, submitted (arXiv:2112.06893). <https://arxiv.org/abs/2112.06893>
- Liu, Z.-W., Stancliffe, R. J., Abate, C., & Matrozos, E. 2017, *ApJ*, 846, 117, doi: [10.3847/1538-4357/aa8622](https://doi.org/10.3847/1538-4357/aa8622)
- Livio, M., Shankar, A., Burkert, A., & Truran, J. W. 1990, *ApJ*, 356, 250, doi: [10.1086/168836](https://doi.org/10.1086/168836)

- Livio, M., & Truran, J. W. 1987, *ApJ*, 318, 316, doi: [10.1086/165369](https://doi.org/10.1086/165369)
- MacDonald, J. 1980, *MNRAS*, 191, 933
- . 1986, *ApJ*, 305, 251, doi: [10.1086/164245](https://doi.org/10.1086/164245)
- MacDonald, J., Fujimoto, M. Y., & Truran, J. W. 1985, *ApJ*, 294, 263, doi: [10.1086/163295](https://doi.org/10.1086/163295)
- MacLeod, M., & Loeb, A. 2020, *ApJ*, 902, 85, doi: [10.3847/1538-4357/abb313](https://doi.org/10.3847/1538-4357/abb313)
- Metzger, B. D., Zenati, Y., Chomiuk, L., Shen, K. J., & Strader, J. 2021, *ApJ*, 923, 100, doi: [10.3847/1538-4357/ac2a39](https://doi.org/10.3847/1538-4357/ac2a39)
- Mikołajewska, J. 2010, arXiv:1011.5657, <https://arxiv.org/abs/1011.5657>
- Nagae, T., Oka, K., Matsuda, T., et al. 2004, *A&A*, 419, 335, doi: [10.1051/0004-6361:20040070](https://doi.org/10.1051/0004-6361:20040070)
- Nelemans, G., Siess, L., Repetto, S., Toonen, S., & Phinney, E. S. 2016, *ApJ*, 817, 69, doi: [10.3847/0004-637X/817/1/69](https://doi.org/10.3847/0004-637X/817/1/69)
- Nelson, T., Mukai, K., Li, K.-L., et al. 2019, *ApJ*, 872, 86, doi: [10.3847/1538-4357/aafb6d](https://doi.org/10.3847/1538-4357/aafb6d)
- Nomoto, K., Saio, H., Kato, M., & Hachisu, I. 2007, *ApJ*, 663, 1269, doi: [10.1086/518465](https://doi.org/10.1086/518465)
- Owoc, S. P., Gayley, K. G., & Shaviv, N. J. 2004, *ApJ*, 616, 525, doi: [10.1086/424910](https://doi.org/10.1086/424910)
- Paczyński, B. 1969, *AcA*, 19, 1
- Pala, A. F., Gänsicke, B. T., Breedt, E., et al. 2020, *MNRAS*, 494, 3799, doi: [10.1093/mnras/staa764](https://doi.org/10.1093/mnras/staa764)
- Pala, A. F., Gänsicke, B. T., Belloni, D., et al. 2022, *MNRAS*, 510, 6110, doi: [10.1093/mnras/stab3449](https://doi.org/10.1093/mnras/stab3449)
- Parker, E. N. 1958, *ApJ*, 128, 664, doi: [10.1086/146579](https://doi.org/10.1086/146579)
- . 1965, *SSRv*, 4, 666, doi: [10.1007/BF00216273](https://doi.org/10.1007/BF00216273)
- Paxton, B., Bildsten, L., Dotter, A., et al. 2011, *ApJS*, 192, 3, doi: [10.1088/0067-0049/192/1/3](https://doi.org/10.1088/0067-0049/192/1/3)
- Paxton, B., Cantiello, M., Arras, P., et al. 2013, *ApJS*, 208, 4, doi: [10.1088/0067-0049/208/1/4](https://doi.org/10.1088/0067-0049/208/1/4)
- Paxton, B., Marchant, P., Schwab, J., et al. 2015, *ApJS*, 220, 15, doi: [10.1088/0067-0049/220/1/15](https://doi.org/10.1088/0067-0049/220/1/15)
- Paxton, B., Schwab, J., Bauer, E. B., et al. 2018, *ApJS*, 234, 34, doi: [10.3847/1538-4365/aaa5a8](https://doi.org/10.3847/1538-4365/aaa5a8)
- Pejcha, O. 2014, *ApJ*, 788, 22, doi: [10.1088/0004-637X/788/1/22](https://doi.org/10.1088/0004-637X/788/1/22)
- Pejcha, O., Metzger, B. D., & Tomida, K. 2016a, *MNRAS*, 455, 4351, doi: [10.1093/mnras/stv2592](https://doi.org/10.1093/mnras/stv2592)
- . 2016b, *MNRAS*, 461, 2527, doi: [10.1093/mnras/stw1481](https://doi.org/10.1093/mnras/stw1481)
- Pejcha, O., Metzger, B. D., Tyles, J. G., & Tomida, K. 2017, *ApJ*, 850, 59, doi: [10.3847/1538-4357/aa95b9](https://doi.org/10.3847/1538-4357/aa95b9)
- Piersanti, L., Cassisi, S., Iben, Jr., I., & Tornambé, A. 2000, *ApJ*, 535, 932, doi: [10.1086/308885](https://doi.org/10.1086/308885)
- Politano, M., Starrfield, S., Truran, J. W., Weiss, A., & Sparks, W. M. 1995, *ApJ*, 448, 807, doi: [10.1086/176009](https://doi.org/10.1086/176009)
- Prialnik, D., & Kovetz, A. 1984, *ApJ*, 281, 367, doi: [10.1086/162107](https://doi.org/10.1086/162107)
- . 1995, *ApJ*, 445, 789, doi: [10.1086/175741](https://doi.org/10.1086/175741)
- Quataert, E., Fernández, R., Kasen, D., Klion, H., & Paxton, B. 2016, *MNRAS*, 458, 1214, doi: [10.1093/mnras/stw365](https://doi.org/10.1093/mnras/stw365)
- Rosner, R., Alexakis, A., Young, Y., Truran, J. W., & Hillebrandt, W. 2001, *ApJL*, 562, L177, doi: [10.1086/338327](https://doi.org/10.1086/338327)
- Saladino, M. I., Pols, O. R., & Abate, C. 2019, *A&A*, 626, A68, doi: [10.1051/0004-6361/201834598](https://doi.org/10.1051/0004-6361/201834598)
- Saladino, M. I., Pols, O. R., van der Helm, E., Pelupessy, I., & Portegies Zwart, S. 2018, *A&A*, 618, A50, doi: [10.1051/0004-6361/201832967](https://doi.org/10.1051/0004-6361/201832967)
- Schaefer, B. E. 2010, *ApJS*, 187, 275, doi: [10.1088/0067-0049/187/2/275](https://doi.org/10.1088/0067-0049/187/2/275)
- Schreiber, M. R., Zorotovic, M., & Wijnen, T. P. G. 2016, *MNRAS*, 455, L16, doi: [10.1093/mnrasl/slv144](https://doi.org/10.1093/mnrasl/slv144)
- Schröder, S. L., MacLeod, M., Ramirez-Ruiz, E., et al. 2021, submitted (arXiv:2107.09675), <https://arxiv.org/abs/2107.09675>
- Schwarz, G. J., Shore, S. N., Starrfield, S., et al. 2001, *MNRAS*, 320, 103, doi: [10.1046/j.1365-8711.2001.03960.x](https://doi.org/10.1046/j.1365-8711.2001.03960.x)
- Shaviv, N. J. 2001, *MNRAS*, 326, 126, doi: [10.1046/j.1365-8711.2001.04574.x](https://doi.org/10.1046/j.1365-8711.2001.04574.x)
- Shen, K. J. 2015, *ApJL*, 805, L6, doi: [10.1088/2041-8205/805/1/L6](https://doi.org/10.1088/2041-8205/805/1/L6)
- Shen, K. J., & Bildsten, L. 2007, *ApJ*, 660, 1444, doi: [10.1086/513457](https://doi.org/10.1086/513457)
- . 2009, *ApJ*, 692, 324, doi: [10.1088/0004-637X/692/1/324](https://doi.org/10.1088/0004-637X/692/1/324)
- Shen, K. J., Idan, I., & Bildsten, L. 2009, *ApJ*, 705, 693, doi: [10.1088/0004-637X/705/1/693](https://doi.org/10.1088/0004-637X/705/1/693)
- Shen, K. J., & Schwab, J. 2017, *ApJ*, 834, 180, doi: [10.3847/1538-4357/834/2/180](https://doi.org/10.3847/1538-4357/834/2/180)
- Shu, F. H., Anderson, L., & Lubow, S. H. 1979, *ApJ*, 229, 223, doi: [10.1086/156948](https://doi.org/10.1086/156948)
- Slavin, A. J., O'Brien, T. J., & Dunlop, J. S. 1995, *MNRAS*, 276, 353, doi: [10.1093/mnras/276.2.353](https://doi.org/10.1093/mnras/276.2.353)
- Sokoloski, J. L., Lawrence, S., Crotts, A. P. S., & Mukai, K. 2017, arXiv:1702.05898, <https://arxiv.org/abs/1702.05898>
- Sokolovsky, K. V., Mukai, K., Chomiuk, L., et al. 2020, *MNRAS*, 497, 2569, doi: [10.1093/mnras/staa2104](https://doi.org/10.1093/mnras/staa2104)
- Starrfield, S., Bose, M., Iliadis, C., et al. 2020, *ApJ*, 895, 70, doi: [10.3847/1538-4357/ab8d23](https://doi.org/10.3847/1538-4357/ab8d23)
- Starrfield, S., Iliadis, C., & Hix, W. R. 2016, *PASP*, 128, 051001, doi: [10.1088/1538-3873/128/963/051001](https://doi.org/10.1088/1538-3873/128/963/051001)
- Starrfield, S., Iliadis, C., Hix, W. R., Timmes, F. X., & Sparks, W. M. 2009, *ApJ*, 692, 1532, doi: [10.1088/0004-637X/692/2/1532](https://doi.org/10.1088/0004-637X/692/2/1532)

- Starrfield, S., Schwarz, G., Truran, J. W., & Sparks, W. M. 2000, in American Institute of Physics Conference Series, Vol. 522, American Institute of Physics Conference Series, ed. S. S. Holt & W. W. Zhang, 379–382, doi: [10.1063/1.1291739](https://doi.org/10.1063/1.1291739)
- Starrfield, S., Truran, J. W., Wiescher, M. C., & Sparks, W. M. 1998, MNRAS, 296, 502, doi: [10.1046/j.1365-8711.1998.01312.x](https://doi.org/10.1046/j.1365-8711.1998.01312.x)
- Strope, R. J., Schaefer, B. E., & Henden, A. A. 2010, AJ, 140, 34, doi: [10.1088/0004-6256/140/1/34](https://doi.org/10.1088/0004-6256/140/1/34)
- Townslley, D. M., & Bildsten, L. 2004, ApJ, 600, 390, doi: [10.1086/379647](https://doi.org/10.1086/379647)
- Weston, J. H. S., Sokoloski, J. L., Metzger, B. D., et al. 2016, MNRAS, 457, 887, doi: [10.1093/mnras/stv3019](https://doi.org/10.1093/mnras/stv3019)
- Wolf, W. M., Bildsten, L., Brooks, J., & Paxton, B. 2013, ApJ, 777, 136, doi: [10.1088/0004-637X/777/2/136](https://doi.org/10.1088/0004-637X/777/2/136)
- Wolf, W. M., Townsend, R. H. D., & Bildsten, L. 2018, ApJ, 855, 127, doi: [10.3847/1538-4357/aaad05](https://doi.org/10.3847/1538-4357/aaad05)
- Woodsley, S. E. 1986, in Nucleosynthesis and Chemical Evolution, ed. B. Hauck, A. Maeder, & G. Meynet (Sauverny: Geneva Observatory), 1
- Yaron, O., Prialnik, D., Shara, M. M., & Kovetz, A. 2005, ApJ, 623, 398, doi: [10.1086/428435](https://doi.org/10.1086/428435)
- Zorotovic, M., Schreiber, M. R., & Gänsicke, B. T. 2011, A&A, 536, A42, doi: [10.1051/0004-6361/201116626](https://doi.org/10.1051/0004-6361/201116626)